







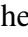



# Quasar Sightline and Galaxy Evolution (QSAGE) – III. The mass–metallicity and fundamental metallicity relation of $z \approx 2.2$ galaxies

H. M. O. Stephenson<sup>1</sup> , <sup>1</sup>★ J. P. Stott<sup>1</sup> , F. Cullen<sup>2</sup> , R. M. Bielby<sup>3</sup> , N. Amos<sup>1</sup> , R. Dutta<sup>4,5</sup> ,  
M. Fumagalli<sup>4,6</sup> , N. Tejos<sup>7</sup> , J. N. Burchett<sup>8,9</sup> , R. A. Crain<sup>10</sup>  and J. X. Prochaska<sup>9</sup>

<sup>1</sup>Department of Physics, Lancaster University, Lancaster LA1 4YB, UK

<sup>2</sup>Institute for Astronomy, University of Edinburgh, Royal Observatory, Edinburgh EH9 3HJ, UK

<sup>3</sup>Department for Education, Bishopsgate House, Feethams, Darlington DL1 5QE, UK

<sup>4</sup>Dipartimento di Fisica G. Occhialini, Università degli Studi di Milano Bicocca, Piazza della Scienza 3, I-20126 Milano, Italy

<sup>5</sup>INAF - Osservatorio Astronomico di Brera, via Bianchi 46, I-23087 Merate (LC), Italy

<sup>6</sup>INAF - Osservatorio Astronomico di Trieste, via G. B. Tiepolo 11, I-34143 Trieste, Italy

<sup>7</sup>Instituto de Física, Pontificia Universidad Católica de Valparaíso, Casilla 4059, Valparaíso, Chile

<sup>8</sup>Department of Astronomy and Astrophysics, UCO/Lick Observatory, University of California, 1156 High Street, Santa Cruz, CA 95064, USA

<sup>9</sup>Department of Astronomy, New Mexico State University, Las Cruces, NM 88003, USA

<sup>10</sup>Astrophysics Research Institute, Liverpool John Moores University, 146 Brownlow Hill, Liverpool L3 5RF, UK

Accepted 2023 November 21. Received 2023 November 10; in original form 2023 August 25

## ABSTRACT

We present analysis of the mass–metallicity relation (MZR) for a sample of 67 [O III]–selected star-forming (SF) galaxies at a redshift range of  $z = 1.99–2.32$  ( $z_{\text{med}} = 2.16$ ) using *Hubble Space Telescope* Wide Field Camera 3 grism spectroscopy from the Quasar Sightline and Galaxy Evolution survey. Metallicities were determined using empirical gas-phase metallicity calibrations based on the strong emission lines [O II]3727, 3729, [O III]4959, 5007 and H $\beta$ . SF galaxies were identified, and distinguished from active-galactic nuclei, via Mass–Excitation diagrams. Using  $z \sim 0$  metallicity calibrations, we observe a negative offset in the  $z = 2.2$  MZR of  $\approx -0.51$  dex in metallicity when compared to locally derived relationships, in agreement with previous literature analysis. A similar offset of  $\approx -0.46$  dex in metallicity is found when using empirical metallicity calibrations that are suitable out to  $z \sim 5$ , though our  $z = 2.2$  MZR, in this case, has a shallower slope. We find agreement between our MZR and those predicted from various galaxy evolution models and simulations. Additionally, we explore the extended fundamental metallicity relation (FMR) which includes an additional dependence on star formation rate. Our results consistently support the existence of the FMR, as well as revealing an offset of  $0.28 \pm 0.04$  dex in metallicity compared to locally derived relationships, consistent with previous studies at similar redshifts. We interpret the negative correlation with SFR at fixed mass, inferred from an FMR existing for our sample, as being caused by the efficient accretion of metal-poor gas fuelling SFR at cosmic noon.

**Key words:** galaxies: evolution – galaxies: ISM – galaxies: star formation.

## 1 INTRODUCTION

Analysis of the relationship between a galaxy’s stellar mass and its gas-phase metallicity (the mass–metallicity relationship, MZR) is a key diagnostic of galaxy evolution, reflecting the complicated interplay between the formation and enrichment of stars and the inflow and outflow of gas in galaxies. The MZR shows that as stellar mass increases, galaxies have enhanced metallicities, with some studies finding the relation flattening at higher masses (e.g. Tremonti et al. 2004; Stott et al. 2013; Zahid et al. 2014; Curti et al. 2020a). The MZR has been studied in the literature for decades. A similar form to the MZR that showed a correlation between the magnitude of a galaxy and its gas-phase metallicity was first observed in the 1970s (Lequeux et al. 1979; Garnett & Shields 1987). Magnitude was used

as a substitute for stellar mass in these early works because of the difficulty in obtaining accurate mass values. Following influential works on stellar evolution (e.g. Charlot & Longhetti 2001; Bruzual & Charlot 2003) and stellar mass determination (e.g. Chabrier 2003; Kauffmann et al. 2003), the MZR has now been fully established in later studies up to at least  $z \sim 3.5$  (e.g. Tremonti et al. 2004; Erb et al. 2006; Mannucci et al. 2010; Stott et al. 2013; Zahid et al. 2014; Ly et al. 2016; Wuyts et al. 2016; Brown et al. 2018; Torrey et al. 2019; Sanders et al. 2021; Suzuki et al. 2021; Wang et al. 2022; Langan et al. 2023; Sextl et al. 2023), as well as the stellar mass–stellar metallicity relation (Cullen et al. 2019, 2021; Kashino et al. 2022). See Maiolino & Mannucci (2019) and references therein for a comprehensive review of the MZR.

The MZR has been extended to include a dependence on star formation rate (SFR). This 3D relationship has been called the fundamental metallicity relation (FMR) and was initially discussed by Ellison et al. (2008), before being expanded upon and fully

\* E-mail: [hmo.stephenson@gmail.com](mailto:hmo.stephenson@gmail.com)

proposed by Mannucci et al. (2010) (see also Lara-López et al. 2010). The FMR suggested by Mannucci et al. (2010) defines a tight relationship that shows gas-phase metallicity strongly decreasing with increasing SFR for low-mass galaxies, but no SFR-dependence on metallicity for high-mass galaxies. Unlike the MZR, there is more debate surrounding the form, and even the existence of, the FMR in galaxies. Sánchez et al. (2013) studied the MZR and FMR using the Calar Alto Legacy Integral Field Area survey (Sánchez et al. 2012) and found that their results contradicted those of Mannucci et al. (2010) (see also Sánchez et al. 2017). Additionally, Barrera-Ballesteros et al. (2017) found no strong relationship between the MZR with SFR (or specific SFR, sSFR) from the Mapping Nearby Galaxies at APO survey (Bundy et al. 2014; Wake 2016), particularly at low SFRs. However, many other studies have found the FMR in star-forming (SF) galaxies at higher redshifts, with suggestions of a redshift evolution compared to local Sloan Digital Sky Survey (SDSS; York et al. 2000; Adelman-McCarthy et al. 2006; Abazajian et al. 2009) galaxies. As well as finding a strong relationship in SDSS galaxies, Mannucci et al. (2010) analysed the FMR in higher  $z$  galaxies from the literature. From their results, they suggest that the FMR exists, but does not evolve, out to  $z \sim 2.5$  for galaxies of any stellar mass and SFR, but a large offset from the trend was found for a sample of  $z \sim 3.3$  galaxies from Maiolino et al. (2008) and Mannucci et al. (2009). Mannucci, Salvaterra & Campisi (2011) built upon the work done by Mannucci et al. (2010) and found a new form of the FMR that extends smoothly down to lower mass SDSS galaxies ( $10^{8.3} M_{\odot}$ , down from a previous minimum of  $\approx 10^{9.2} M_{\odot}$ ) by studying the properties of long gamma-ray burst hosts. Utilizing the grism technology of the *Hubble Space Telescope* (HST) in the 3D-HST survey (Brammer et al. 2012), Cullen et al. (2014) found the FMR in their  $z \sim 2.16$  galaxies but they were offset from the Mannucci et al. (2010) FMR by 0.3 dex, suggesting that an evolution in the ionization conditions between the redshifts of the samples affected the metallicity calibrations, and that the choice of metallicity indicator may affect measured values of gas-phase metallicity (see also Teklu et al. 2020 for the latter conclusion). More recently, Li et al. (2023) used the capabilities of the *James Webb Space Telescope* (JWST) to study the MZR in dwarf galaxies between  $z = 2$  and 3 and found the FMR exists for a mass range  $10^6 - 10^{10} M_{\odot}$  in a marginally different form than observed by Mannucci et al. (2010), but one that is in close agreement with other studies at this redshift (see Sanders et al. 2021). Evidence is increasing that the MZR does have a secondary dependence with SFR (e.g. Yates, Kauffmann & Guo 2012; Andrews & Martini 2013; Stott et al. 2013; Salim et al. 2014, 2015; Cresci, Mannucci & Curti 2019; Curti et al. 2020a; Baker et al. 2022; Schaefer et al. 2022). The FMR provides a more complete picture of the processes that regulate galaxy evolution, as it accounts for the fact that there is a relationship between SFR and gas-phase metallicity at a fixed stellar mass. Further investigation of the FMR is paramount for understanding the complex mechanisms that link star formation and chemical evolution in galaxies.

The origins of the MZR and FMR are still not fully understood, and several models have been proposed to explain their existence. These include inflows and outflows of both metal-enriched (Edmunds 1990; Spitoni et al. 2010; Spitoni, Vincenzo & Matteucci 2017; Saracco et al. 2023) and metal-poor (including pristine) gas (Finlator & Davé 2008; Davé et al. 2010; Jimmy et al. 2015), as well as feedback from supernovae (Sakstein et al. 2011; Collacchioni et al. 2018) and active galactic nuclei (AGN) (Torrey et al. 2019; van Loon, Mitchell & Schaye 2021; Yang, Scholte & Saintonge 2022). Additionally, recent observations and simulations have suggested that the MZR also has a secondary dependence on gas mass (Brown et al. 2018; De Lucia

et al. 2020), with some claiming that it is the more fundamental property linked to mass and gas-phase metallicity, and that SFR is simply a tracer for gas mass in the FMR (Scholte & Saintonge 2022). In particular, studies have suggested that the secondary dependence is with HI mass or neutral gas fraction, as the relationship between gas-phase metallicity and SFR could be a by-product of the dependence on gas density via the Kennicutt–Schmidt relation (Bothwell et al. 2013; Lagos et al. 2016; De Rossi et al. 2017). Recently, however, Baker & Maiolino (2023) conclude that it is in fact stellar mass that is the primary property that drives the gas-phase metallicity in galaxies, ahead of any other galaxy property including SFR, velocity dispersion and dynamical mass. Furthermore, they find that not only does gas-phase metallicity have no other significant dependence when stellar mass is included, it potentially has an anticorrelation with dynamical mass at fixed stellar mass once the primary dependence has been accounted for.

The evolution of the MZR and FMR with redshift is also an active area of research, as it can provide insights into the formation and evolution of galaxies during certain epochs of the Universe's lifetime. Several studies have investigated this and the results are mixed. Both Savaglio et al. (2005) and Erb et al. (2006) found offsets from the MZR in  $z = 1-2$  galaxies compared to the local  $z \sim 0.1$  MZR suggested by Tremonti et al. (2004). Similar offsets from local calibrations have been repeated in many later studies (e.g. Maiolino et al. 2008; Curti et al. 2022). Given the proposed existence of the FMR (see above), Baker & Maiolino (2023) suggest that any offset likely arises from the fact the MZR is tracing the SFR evolution with redshift (Madau & Dickinson 2014). However, as previously mentioned, Mannucci et al. (2010) found no redshift evolution in the FMR out to  $z \sim 2.5$  but a large offset for their  $z > 3$  sample, whereas Cullen et al. (2014) did find an offset at  $z \sim 2.16$ . Results from other studies have shown that there is no evolution in the FMR out to  $z \sim 2-2.5$  (e.g. Henry et al. 2013; Barrera-Ballesteros et al. 2017), and others back only a mild evolution with redshift (e.g. Baker et al. 2022).

Some studies suggest any perceived evolution in the FMR toward higher redshifts is a result of the choice of metallicity calibration, specifically those developed using samples of low- $z$  galaxies that may not be applicable for sources at high- $z$ . Many of these calibrations use emission-line diagnostics (Maiolino et al. 2008; Dopita et al. 2016; Bian, Kewley & Dopita 2018). In their review on the use of emission lines to study galaxy evolution, Kewley, Nicholls & Sutherland (2019) emphasize the need for reliable emission line diagnostics to accurately determine fundamental properties of galaxies, including their metallicities. Some of the challenges they discuss include the limited number of emission lines available to some studies, the changing ionization structure of HII regions and the interstellar medium (ISM), and contamination from shock excitation (see Kewley, Nicholls & Sutherland 2019 for a detailed review). Some studies have sought to develop metallicity calibrations that are independent of these problems, such as Dopita et al. (2016), who developed a calibration that relies only on [N II]6585, [S II]6717, 6732 and H $\alpha$  emission lines which relieves the issues caused by ISM pressure and ionization parameter. Cullen et al. (2014) concluded that offsets from the FMR of their sample mentioned above are likely down to the empirical Maiolino et al. (2008) metallicity calibrations – derived from local SDSS galaxies – not being applicable for their  $z \gtrsim 2$  sample, as they do not account for changes in ionization conditions in SF galaxies. Recently, Garg et al. (2023) used the SIMBA hydrodynamical cosmological galaxy formation simulations (Davé et al. 2019) and photoionization modelling (Ferland et al. 2017; Garg et al. 2022) to analyse the redshift evolution of a number of

emission line ratios used as metallicity indicators. They found that all of the emission lines they study, which are typically calibrated on  $z = 0$  populations of galaxies, do have some evolution with redshift, suggesting that as the galactic properties they use in their models evolve with redshift, they have a discernible impact on the line ratios. Further studies have found that metallicities of high- $z$  SF galaxies determined from locally derived strong-line calibrations are offset from the tight sequence found in BPT diagrams of galaxies at the same redshift, suggesting some systematic offset due to the choice of calibration (Steidel et al. 2014; Shapley et al. 2015; Bian, Kewley & Dopita 2018).

The work in this paper aims to contribute to our understanding of the MZR and FMR by exploring them in a sample of SF galaxies at  $z = 1.99–2.34$  ( $z_{\text{median}} = 2.16$ ) using near-infrared (NIR) *HST* grism data from the Quasar Sightline and Galaxy Evolution (QSAGE) survey (Bielby et al. 2019). The QSAGE survey was designed to obtain hundreds of galaxy redshifts by centring *HST*’s Wide-Field Camera 3 (WFC3) on 12 known quasars, all of which with pre-existing *HST* UV spectra. Focussing on quasar sightline-selected fields allows the circumgalactic medium (CGM) of galaxies that are not subject to any selection effects to be studied in detail (Bielby et al. 2019). This data can be used to further develop models of galaxy feedback and fuelling mechanisms associated with the CGM (see e.g. Bielby et al. 2017) and investigate the effect of galaxy environments on the CGM (see e.g. Dutta et al. 2021). However, in this paper, we study galaxies that are generally at higher  $z$  than the quasars.

This paper is arranged as follows. In Section 2, the QSAGE survey is described and the sample used for this work, including how the data was reduced, is explained in detail. The methods for determining galaxy properties, namely stellar mass values (Section 2.3.1) and SFRs (Section 2.3.2), can be found in Section 2.3. Section 3 provides an overview of the Mass–Excitation (MEx) diagram, which was used to distinguish between AGN and SF galaxy populations. Details on the metallicity calibrations used for our sample of galaxies, namely those from Maiolino et al. (2008) and Bian, Kewley & Dopita (2018), are found in Section 4.1 and 4.2, respectively. The results are outlined in Section 5. Discussion and conclusions are summarized in Section 6.

A standard Lambda cold dark matter cosmology model is assumed with values  $\Omega_{\Lambda} = 0.7$ ,  $\Omega_{\text{m}} = 0.3$ , and  $H_0 = 70 \text{ km s}^{-1} \text{ Mpc}^{-1}$ . Any magnitudes stated are presented using the AB system. All results and models in this work assume a Chabrier (2003) initial mass function (IMF) throughout and any comparison results that use a different IMF (i.e. Salpeter 1955; Kroupa 2001) are converted accordingly.

## 2 SAMPLE AND DATA

### 2.1 QSAGE

The data used for the analysis in this paper was taken from the QSAGE survey (*HST* Cycle 24 Large Program 14594; PIs: R. Bielby, J. P. Stott; see Bielby et al. 2019 and Stott et al. 2020). The QSAGE survey’s main science goal was to obtain redshifts for galaxies along the lines of sight to quasars with pre-existing UV spectra in a redshift range  $z = 1.2–2.4$ , with the main aim of analysing the galaxies’ CGM. The survey utilized the capabilities of *HST*’s WFC3 instrument, particularly the IR G141 grism, which provides useful spectra in the range of  $\lambda = 10\,750–17\,000 \text{ Å}$ , and also imaging from the *F140W* and *F160W* filters with spectral ranges of  $\lambda = 11\,854–16\,129 \text{ Å}$ , and  $13\,854–16\,999 \text{ Å}$ , respectively. Each target quasar field was observed with 16 grism exposures lasting

approximately 1000 seconds, as well as eight  $\approx 250 \text{ s}$  exposures in both the *F140W* and *F160W* filters, across a total of eight *HST* orbits. The G141 grism observations are the primary focus of the survey, as they provide spectroscopic data for potentially hundreds of objects simultaneously, allowing for analysis of both foreground and background galaxies around the target quasar. Imaging data, mainly from the *F140W* filter which has a similar spectral range to G141, is used to provide source coordinates for extracting the object spectra. As grism spectra will inevitably include contamination from nearby sources, the survey includes four separate *HST* roll angles for the grism observations as well as a quantitative estimate of the contamination for each source using GRIZLI (Brammer 2019). Table 1 includes the location of the quasar fields in the QSAGE survey and an upper limit on the number of  $z \sim 2.2$  SF galaxies found in the images of each (see Section 3 for explanations of ‘upper limit’ and what defines an SF galaxy in this work).

### 2.2 Sample selection

In order to select only those  $z \sim 2.2$  objects relevant to the analysis in this work, the following criteria must be met:

- (i) The objects are primarily selected based on their [O III]5007 emission. [O III]5007 emission flux was chosen as the primary selection criterion because this line is much stronger compared to other lines at the target redshift of this paper (namely [O II]3727 and  $\text{H}\beta$ ). Therefore, the objects must have a clean spectrum with [O III]5007 coverage. Given the need for multiple emission lines to determine gas-phase metallicity and distinguish ionization processes, objects must also have a spectroscopic [O III]5007 redshift that puts [O II]3727 and  $\text{H}\beta$  within the wavelength range of the G141 grism. The definition of ‘clean spectrum’ is explained by Stott et al. (2020) as being galaxies with a ‘quality flag’ of 3 or 4. As defined in Stott et al. (2020), ‘3’ is a good-quality spectrum with at least one spectral line having  $\text{S/N} > 3$ , and ‘4’ is spectrum with lines that have  $\text{S/N} > 10$ . This cut was necessary in order to make sure that any emission line of an object could be reliably used when calibrating its gas-phase metallicity and used in ionization mechanism diagnostics (see Section 3).
- (ii) Additionally, objects must have an [O III]5007 emission line flux with a signal-to-noise ratio ( $\text{S/N}$ )  $\geq 3$ .  $\text{S/N}$  here is defined as the [O III]5007 flux value over the flux error.

These selection criteria cut the original sample of 1953 objects down to 153. It was clear, however, that this new sample was incomplete for lower valued bins in both [O III]5007 flux and stellar mass, so an additional completeness limit was then applied to this sample of 153 objects. In this case, that was any object with  $\log_{10}(f[\text{O III}]5007) \text{ erg}^{-1} \text{ cm}^{-2} \gtrsim -16.2$  and  $\log_{10}(M_*/M_{\odot}) \gtrsim 9.4$ , which are the lower values of the most occupied bin in each property (see Fig. 1). The [O III]5007 flux and stellar mass distribution of this sample of selected objects, as well as the completeness limit, can be seen in Fig. 1. Statistical analysis found that both the stellar mass and [O III]5007 flux cuts represent an  $\sim 95$  per cent completeness limit of the original sample. After applying these, there were 92 objects in total for analysis within a redshift range of  $1.99 \leq z \leq 2.32$ .

### 2.3 Galaxy Properties

#### 2.3.1 Galaxy stellar mass calibration

The QSAGE masses are inferred using an approximation based on their apparent magnitude in the IR. For this study, the calibrations

**Table 1.** The QSAGE sample. Field name is the name of the central quasar of each observation but here refers to the target field for the SF galaxies.

Field name	RA	Dec.	Number of SF galaxies	SF galaxies $z$ range
QSO-J1130-1449	11:30:07.1	-14:49:27.4	3	2.29–2.32
LBQS-1435-0134	14:37:48.3	-01:47:10.8	8	2.00–2.23
QSO-B1521+1009	15:24:24.5	+09:58:29.1	11	2.03–2.28
QSO-B1634+7037	16:34:29.0	+70:31:32.4	3	2.16–2.17
PKS-0232-04	02:35:07.3	-04:02:05.3	5	2.18–2.32
QSO-B1630+3744	16:32:01.1	+37:37:50.0	4	2.06–2.21
PG0117+213	01:20:17.3	+21:33:46.2	3	2.12–2.13
QSO-B0810+2554	08:13:31.3	+25:45:03.1	5	2.15–2.30
HE0515-4414	05:17:07.6	-44:10:55.6	5	1.99–2.30
2QSO-B0747+4259	07:50:54.6	+42:52:19.3	3	2.02–2.26
QSO-J1019+2745	10:19:56.6	+27:44:01.7	12	2.02–2.24
QSO-B1122-168	11:24:42.9	-17:05:17.4	5	2.03–2.16

*Notes.* The right ascension (RA) and declination (Dec.) of the target quasar are derived by Stott et al. (2020). The number of  $z \sim 2.2$  SF galaxies in each field (number of SF galaxies) refers to the number of objects within the completeness limits of the sample that are deemed to satisfy the definition of SF via the Coil et al. (2015) MEx diagram diagnostic (see Section 3).

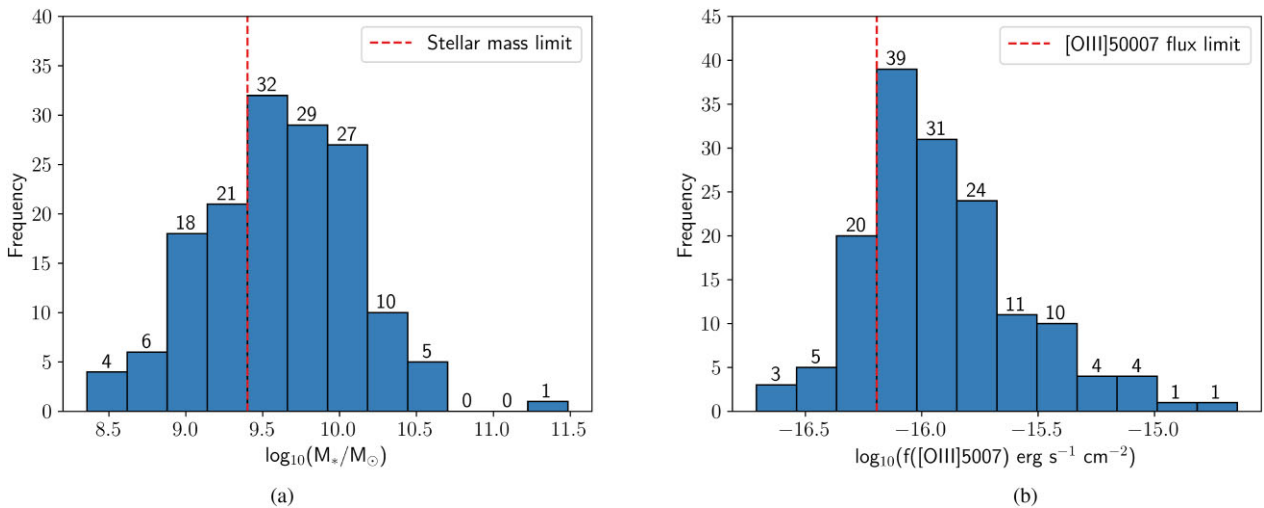


**Figure 1.** The stellar mass and [O III]5007 flux distributions of the objects that met the selection criteria in Section 2.2. Left panel: The stellar mass distribution of the sample, where the red-dashed line indicates the approximate mass-complete limit of the sample  $\sim 10^{9.4} M_\odot$ . Right panel: The [O III]5007 flux distribution of the sample, where the red-dashed line indicates the flux-complete limit of the sample  $\sim 10^{-16.2} \text{ erg s}^{-1} \text{ cm}^{-2}$ . The numbers above each bin indicate the number of objects that occupy that bin.

from Stott et al. (2020) are used. They found linear relationships between stellar mass and  $F160W$  magnitude at different redshifts based on galaxies from the Cosmic Assembly Near-infrared Deep Extragalactic Legacy Survey (CANDELS; Barro et al. 2019). They derive the relationships in individual redshift bins of  $\Delta z = 0.1$ . The parameters they use can be found in Table A1 of their paper. Of the 92 objects in our complete sample, two do not have  $F160W$  coverage (both found in the QSO-J1130-1449 field). The  $F160W$  magnitudes for these two objects were estimated based on a linear fit between the  $F140W$  and  $F160W$  magnitudes of all the  $z \sim 2.2$  objects with a spectra flagged as ‘good’.

As described above, Stott et al. (2020) demonstrate a strong correlation between  $F160W$  and full SED-fit stellar mass for SF galaxies in the CANDELS survey. In the absence of deep homogeneous data across all 12 of the QSAGE fields, we chose to use this  $F160W$  magnitude calibration (corresponding to rest-frame  $V$  band). This is redward of the 4000 Å break and is therefore less affected by ongoing SF than shorter wavelengths. The primary samples we use to analyse the MZR and FMR are all SF galaxies, which means they will all have similar mass-to-light ratios. We fully account for the

scatter in the Stott et al. (2020) relationship in our stellar mass errors (typical stellar mass error can be seen in the lower right corner of Fig. 4).

### 2.3.2 Determining SFRs

The FMR describes the dependence of gas-phase metallicity on both stellar mass and SFR (Ellison et al. 2008; Mannucci et al. 2010). In order to analyse the FMR using the samples in this work, the SFRs of each galaxy are needed. The SFRs were calculated using the Kennicutt (1998) calibrations, making sure to convert from a Salpeter (1955) to a Chabrier (2003) IMF by dividing the resulting SFR by a conversion factor of 1.59 (Madau & Dickinson 2014). SFR was calculated using the  $H\beta$  line luminosity, and then using the common conversion factor of  $H\alpha/H\beta = 2.86$  (Gaskell & Ferland 1984; Osterbrock & Ferland 2006) to estimate the SFR. The theoretical value of the Balmer decrement  $H\alpha/H\beta = 2.86$  is used as the spectra in our sample do not have  $H\alpha$  coverage at this redshift. The emission line luminosity was extinction corrected assuming  $A_V = 1$ , which, based on the properties of our sample, was most appropriate following the



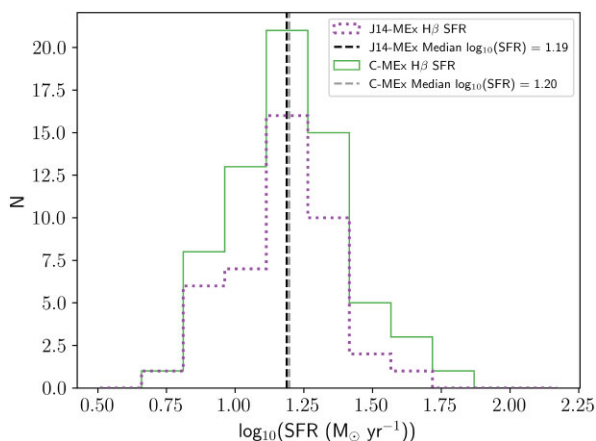


**Figure 2.** The SFR distribution of our complete J14-MEx (purple-dotted histogram) and C-MEx (solid green histogram) SF galaxy samples. The dashed black line indicates the median SFR of our J14-MEx sample, and the grey-dashed line shows the median SFR of the C-MEx sample. The SFR distributions were derived using the  $H\beta$  emission line flux (Kennicutt 1998).

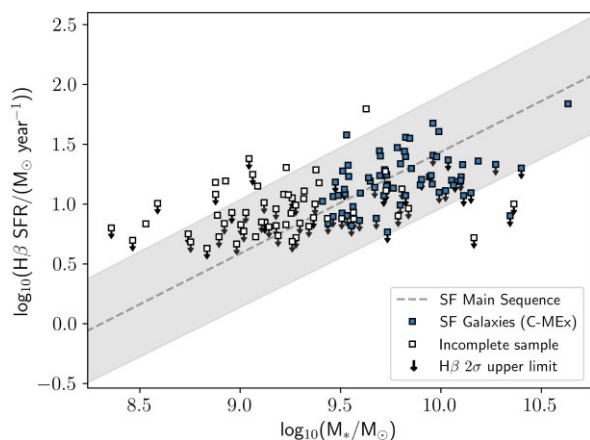


**Figure 3.** The relationship between stellar mass and SFR for the SF galaxies in our C-MEx sample. The grey-dashed line shows the ‘UV + IR/IR’ SF main sequence as described by Speagle et al. (2014), with the grey-shaded region indicating the scatter around the fit based on the errors of their equation. The blue squares show the individual galaxies in the mass and flux complete sample of our work, with white squares showing SF galaxies in the incomplete sample.

extinction relationships of Sobral et al. (2012). In order to correct for underlying stellar absorption,  $H\beta$  flux values were boosted by 3 per cent, in line with other studies into the FMR (Henry et al. 2013; Cullen et al. 2021; Sanders et al. 2021; Curti et al. 2022). These SFRs, calculated using the  $H\alpha$  calibration from Kennicutt (1998), will be referred to as  $H\beta$  SFR hereafter. The SFR distribution of our sample can be found in Fig. 2.

Fig. 3 shows the correlation between SFR and stellar mass for individual SF galaxies in our sample. The grey-dashed line shows the ‘UV + IR/IR SFRs’ best-fitting main-sequence evolution for galaxies out to  $z \approx 6$  as found by Speagle et al. (2014), with the grey-shaded region indicating the scatter based on the errors on their relationship. From Fig. 3, our sample is consistent with the main sequence from Speagle et al. (2014).

### 3 MASS-EXCITATION DIAGRAM

The selection criteria listed in Section 2.2 do not distinguish between object spectra that belong to an AGN or those that belong to SF galaxies – the primary target of the analysis in this paper. Therefore, diagnostics to differentiate the two populations must be employed so as to not contaminate the sample. Traditionally, researchers have used ‘BPT’ diagrams (Baldwin, Phillips & Terlevich 1981) to distinguish between AGN and SF galaxies. These diagrams use different emission line ratios to distinguish the ionization mechanism of gas in the ISM. However, as previously discussed, the emission lines used in our analysis are  $[O\text{III}]\lambda 4959$ ,  $5007$ ,  $[O\text{II}]\lambda 3727$  and  $H\beta$  and therefore no form of BPT diagram can be used to categorize these populations.

Juneau et al. (2011) discovered that comparing the line ratio  $[O\text{III}]\lambda 5007/H\beta$  (hereafter O3) against the total stellar mass of the object is successful at distinguishing between ionization from AGN and that from active SF. They call this the MEx diagram which finds that the BPT–SF and BPT–AGN classifications are well separated in this plane, including finding that BPT-composites (populations that have some combination of SF and AGN contributions) are reasonably well defined in a central region known as ‘MEx-intermediates’. The distinct classes in the MEx diagram come from two empirical curves that maximize this separation. However, Juneau et al. (2011) note that this diagnostic was only applied at intermediate redshifts ( $0.3 < z < 1$ ) and may not be accurate for higher redshift samples. Studies have found that the Juneau et al. (2011) MEx diagram (hereafter J11-MEx) does hold up to  $z \lesssim 1.6$  (e.g. Juneau et al. 2013; Trump et al. 2013), but it generally fails at accurately distinguishing SF galaxies from AGN at  $z \sim 2$  (e.g. Henry et al. 2013; Newman et al. 2013).

While Juneau et al. (2011) used an S/N criterion that applied to the individual emission lines (requiring  $S/N > 3$  on all lines), Juneau et al. (2014) developed a new MEx diagram (hereafter J14-MEx) which instead requires all line ratios to have an  $S/N > 3/\sqrt{2} \approx 2.12$  (equivalent to an average  $3\sigma$  detection at the lower limit for the individual lines in the ratio), resulting in a 20 per cent larger sample. Additionally, Juneau et al. (2014) make use of SDSS DR7 (Abazajian et al. 2009) for their low-redshift sample, rather than SDSS DR4 (Adelman-McCarthy et al. 2006) used for the original J11-MEx. However, the most important update to the J14-MEx is its application to higher redshift samples ( $z \gtrsim 2$ ) by taking into account the evolution of galaxy populations, in particular, the fading of the luminosity function of emission-line galaxies toward lower redshifts (e.g. Colbert et al. 2013; Khostovan et al. 2015; Hayashi et al. 2020). They find that as the cut-off line luminosity is raised, the split between AGN and SF galaxies occurs at higher masses and so they employ a mass-offset as a function of the threshold line luminosity of a sample following the form

$$\Delta \log_{10}(M_*/M_\odot) = a_0 + a_1 \times \tan^{-1}((\log_{10}(L_{\text{threshold}}) - a_2) \times a_3),$$

with coefficients  $\{0.28988, 0.28256, 40.479, \text{ and } 0.82960\}$ . Using the line flux limit of the QSAGE survey ( $f > 2 \times 10^{-17} \text{ erg cm}^{-2}$ ; Bielby et al. 2019) and the median redshift of our complete sample ( $z \sim 2.16$ ), the mass offset on the J14-MEx for this sample is  $\Delta \log_{10}(M_*/M_\odot) \approx 0.25$  which agrees with offsets calculated by other studies with similar flux limits and redshifts (e.g. Coil et al. 2015).

This mass shift of 0.25 dex may be insufficient to clearly separate high- $z$  AGN and SF galaxies, despite the prescriptions in Juneau et al. (2014). Coil et al. (2015) also found a shift of 0.25 dex to the MEx diagram for their sample but found that this shift still leaves many known SF galaxies in the AGN region (see their Fig. 5). Instead, Coil et al. (2015) found that a shift of  $\Delta \log_{10}(M_*/M_\odot) =$

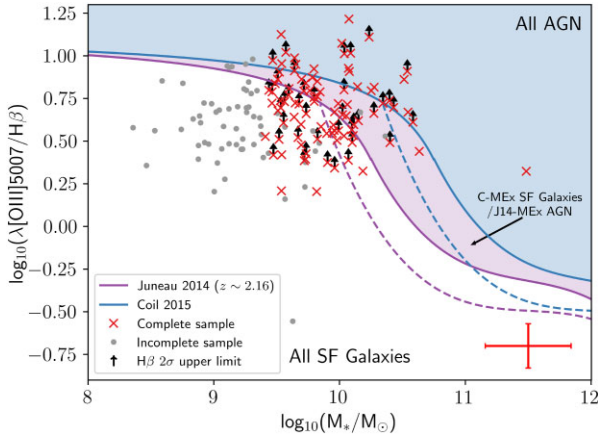


**Figure 4.** The MEx diagram used to distinguish between ionization from AGN and that from SF. The red crosses are objects that are within the completeness limits of both stellar mass and [O III]5007 flux, and grey points are those that lie outside of one or both. Black arrows indicate those objects in our complete sample that have a H $\beta$  upper limit (lower limit on O3). Both of the curves show the MEx prescriptions used to distinguish ionization processes for our sample, namely the mass-shifted (0.25 dex) Juneau et al. (2014) curve that is more applicable to higher redshifts (purple), and the Coil et al. (2015) curve (blue) that shifted the Juneau et al. (2014) curve further (0.75 dex). The area in-between the dashed and solid curves indicates a population of ‘MEx-intermediates’ where there is some combination of SF and AGN activity (analogous to BPT-composites which are reasonably well-defined in this region). For our samples, we considered these MEx-intermediates to be SF galaxies. Objects occupying the unshaded region below the solid Juneau et al. (2014) MEx curve are always considered SF galaxies, and objects occupying the blue-shaded region above the solid Coil et al. (2015) MEx curve are always considered AGN. In the purple-shaded region between the two curves, objects are considered to be SF galaxies for the C-MEx diagnostic (because they lie below the solid blue curve), but are considered to be AGN for the shifted J14-MEx (because they lie above the solid purple line). The red error bars in the bottom right corner show the typical errors of the objects.

0.75 is needed and results in all ten of their X-ray and IR-selected AGN being consistent with occupying the AGN region of the J14-MEx diagram. They note that other studies with samples at a similar redshift (e.g. Newman et al. 2013; Price et al. 2014) found that a similarly substantial shift of 0.75 dex is needed for the original J11-MEx, suggesting the prescriptions in Juneau et al. (2014) are generally insufficient for samples at  $z \gtrsim 2$ . For completeness, the analysis of the MZR and FMR in this study will look at samples of SF galaxies determined using both a 0.25 and 0.75 dex shift to the Juneau et al. (2014) prescriptions (43 and 67 SF galaxies, respectively), with the primary focus being on the Coil et al. (2015) 0.75 dex shift (hereafter the C-MEx sample). Fig. 4 shows the MEx diagram for the sample of objects in this paper with both the shifted Juneau et al. (2014) and Coil et al. (2015) curves discussed in this section highlighted. For the purposes of this paper, an object was considered an SF galaxy if it was below the upper solid line of the empirical curves, including those that would otherwise be considered as MEx-intermediates. We used a  $2\sigma$  upper limit on the value of H $\beta$  here (lower limit on O3) where the S/N < 2, which means the number of SF galaxies determined via this method is also an upper limit.

The stellar mass range of our J14-MEx sample of 43 SF galaxies is  $M_* = 10^{9.41} - 10^{10.19} M_\odot$  (median stellar mass  $M_* = 10^{9.70} M_\odot$ ), and the range for our C-MEx sample of 67 SF galaxies is  $M_* = 10^{9.41} - 10^{10.63} M_\odot$  (median stellar mass  $M_* = 10^{9.80} M_\odot$ ). The SFR range of our J14-MEx sample is 5.8–37.7  $M_\odot \text{yr}^{-1}$  (median

SFR of 15.4  $M_\odot \text{yr}^{-1}$ ), and the range for our C-MEx sample is 5.8–68.9  $M_\odot \text{yr}^{-1}$  (median SFR of 15.7  $M_\odot \text{yr}^{-1}$ ).

#### 4 DETERMINING GAS-PHASE METALLICITY

Gas-phase metallicity at high redshifts ( $z > 1$ ) could only be properly determined using strong-line metallicity diagnostics, as measurements of the electron temperature ( $T_e$ , often used to directly measure metallicities in local galaxies) become difficult due to the faintness of temperature-sensitive emission lines (Sanders et al. 2020). However, the resolution and spectroscopic capabilities of *JWST* are now making this possible (e.g. Curti et al. 2022; Sanders et al. 2023), meaning studies using it will not necessarily have to rely on strong-line calibrations to measure metallicity of these high- $z$  galaxies. Strong-line diagnostics follow the relationship between optical emission line ratios and the abundance of heavy elements in a galaxy. It is important to note that analysis into the MZR (or other metallicity relations) is strongly dependant on the choice of calibration as it can result in significantly different curve shapes and intercepts (see Kewley & Ellison 2008 for a detailed review). It is therefore crucial to use the same metallicity calibration as those comparison studies. Here, two-key calibrations are adopted for analysing the MZR and FMR. They are the calibration curves from Maiolino et al. (2008), who developed strong-line relations from a combination of metallicities measured using the  $T_e$  method in Nagao, Maiolino & Marconi (2006) and photoionization models on SDSS DR4 galaxies (Adelman-McCarthy et al. 2006), and those from Bian, Kewley & Dopita (2018), who developed empirical calibrations from local galaxies with properties analogous to galaxies at  $z \sim 2$ .

##### 4.1 Maiolino et al. (2008) calibrations

The Maiolino et al. (2008) calibrations were needed in order to compare the MZR and FMR determined for our sample to those by Mannucci et al. (2010) and Cullen et al. (2014). As described above, Maiolino et al. (2008) used a combination of directly measured metallicities via the  $T_e$  method and photoionization models. However, it is well documented that the  $T_e$  method fails at high metallicities (reliable for  $12 + \log_{10}(\text{O}/\text{H}) \lesssim 8.3$ , see Stasińska 2005; Bresolin 2007) as a result of temperature fluctuations. Photoionization models are also prone to systematic effects as well as high uncertainties and often do not reliably reproduce expected trends at low metallicities (e.g. Dopita et al. 2006; Dors Jr et al. 2011). Therefore, Maiolino et al. (2008) combine a low-metallicity sample from Nagao, Maiolino & Marconi (2006) that used direct gas-phase metallicity measurements via  $T_e$ , and a high-metallicity sample using galaxies from SDSS DR4 (Adelman-McCarthy et al. 2006) with the photoionization models described in Kewley & Dopita (2002). They then fitted polynomial curves to various strong-line ratio relationships against gas-phase metallicity after binning the galaxies in  $\sim 0.1$  dex metallicity bins. The key relationships for our sample were those using  $R_{23} = ([\text{O III}]5007 + [\text{O III}]4959 + [\text{O II}]3727)/\text{H}\beta$ ,  $[\text{O III}]5007/[\text{O II}]3727$  (herein O32),  $[\text{O II}]3727/\text{H}\beta$  (herein O2) and O3. For the [O III]4959, 5007 doublet, the QSAGE team fitted a triple Gaussian to determine the line flux. However, due to the grism’s spectral resolution constraints, the peaks are only marginally resolved in most spectra and so a fixed flux ratio of  $[\text{O III}]5007/[\text{O III}]4959 = 2.98$  was assumed (Storey & Zeippen 2000). This fit also included H $\beta$  ( $\lambda = 4861 \text{ \AA}$ ) since its close proximity may have led to some blending (Stott et al. 2020). The

general form of the polynomials fitted by Maiolino et al. (2008) is

$$\log_{10}(R) = c_0 + c_1x + c_2x^2 + c_3x^3 + c_4x^4, \quad (1)$$

where  $R$  is the strong-line ratio,  $x = 12 + \log_{10}(\text{O}/\text{H}) - 8.69$  and  $c_n$  are coefficients that depend on the chosen ratio (see table 4 in Maiolino et al. 2008).

We calibrated metallicities by following a  $\chi^2$  minimization approach adopted by Sanders et al. (2021) (see also Cullen et al. 2021; Curti et al. 2023). This method involves minimizing the  $\chi^2$  of multiple line ratios simultaneously using the formula

$$\chi^2(x) = \sum_i \frac{(R_{\text{obs},i} - R_{\text{cal},i}(x))^2}{(\sigma_{\text{obs},i}^2 + \sigma_{\text{cal},i}^2)}, \quad (2)$$

where the sum over  $i$  represents the set of the line ratios used for the gas-phase metallicity determination,  $x = 12 + \log_{10}(\text{O}/\text{H})$ ,  $R_{\text{obs},i}$  is the logarithm of the  $i$ th observed line ratio,  $R_{\text{cal},i}(x)$  is the predicted logarithmic value of  $R_i$  at  $x$  from the Maiolino et al. (2008) calibrations,  $\sigma_{\text{obs},i}$  is the uncertainty in the  $i$ th observed line ratio, and  $\sigma_{\text{cal},i}$  is the uncertainty of the  $i$ th line ratio at a fixed  $x$  of the Maiolino et al. (2008) calibrations. For  $\sigma_{\text{cal},i}$ , we used the values from Table 2 of Sanders et al. (2021) which are the average values for multiple calibrations (including Maiolino et al. 2008), but they note that all of them have similar scatter for each of the line ratios used. Metallicities were calculated by selecting the value that minimized Equation (2). To determine the uncertainty of the gas-phase metallicity, we followed the method of Cullen et al. (2021); the observed line ratios were perturbed by their uncertainty values using a Gaussian distribution and the metallicity that minimized Equation (2) was recalculated 500 times. The  $1\sigma$  uncertainty on the calculated metallicity was then derived from the 68th percentile width of the resulting distribution of perturbed metallicities.

Since [O II]3727 and H $\beta$  may be undetected in the QSAGE sample ( $S/N < 2$ ), the strong-line ratios used to calibrate the gas-phase metallicity must be carefully chosen. The reader should be reminded that [O III]5007 is detected to  $S/N > 3$  in all cases (see Section 2.2). The selection process for the ratio(s) used in Equation (2) is as follows:

- i) If [O II]3727 and H $\beta$  are both detected with  $S/N \geq 2$ , then all of  $R_{23}$ , O3, O2, and O32 are used in Equation (2) (applies to 28/67 C-MEx SF galaxies).
- ii) If [O II]3727 is poorly detected ( $S/N < 2$ ) but H $\beta$  is well detected ( $S/N \geq 2$ ), then only O3 is used (9/67 C-MEx SF galaxies).
- iii) If H $\beta$  is poorly detected ( $S/N < 2$ ) but [O II]3727 is well detected ( $S/N \geq 2$ ), then only O32 is used (26/67 C-MEx SF galaxies).
- iv) In the event that both H $\beta$  and [O II]3727 are poorly detected ( $S/N < 2$ ), then the  $\chi^2$  minimization method is not followed. Instead, we solve Equation (1) using O32 with an upper limit on [O II]3727 (4/67 C-MEx SF galaxies). The upper limit was applied as follows: if [O II]3727 flux was poorly detected (i.e.  $0 < S/N < 2$ ), then the flux was corrected to double the value of the uncertainty on the measurement, i.e. a  $2\sigma$  upper limit. If no [O II]3727 was detected, then the [O II]3727 flux value was set to be double the value of the corresponding [O III]5007 flux error for that object; if the [O II]3727 upper limit results in an O32 value that is on the curve described by Equation (1), then this metallicity was selected (upper limit on metallicity). Should an object have an O32 value that is above the curve, then the metallicity corresponding to the maximum strong-line ratio on the curve would have been selected (and these noted with extreme caution as having a lower metallicity limit), but there were no such cases in this sample.

Since some of the curves defined by Equation (1) have multiple solutions, O32 was used to discriminate between them since the shape of the O32 curve in the metallicity range  $7 \lesssim 12 + \log_{10}(\text{O}/\text{H}) \lesssim 9.5$  has a single solution.

#### 4.2 Bian et al. (2018) calibrations

To compare our MZR and FMR results to higher redshift studies, we need to adopt the higher redshift metallicity calibrations these studies used. We primarily look at the FMR of Li et al. (2023), who recently analysed the gas-phase metallicity of galaxies at  $z = 2-3$  using *JWST* (also to their MZR, see Section 5.1). In order to compare to Li et al. (2023), the metallicity calibrations from Bian, Kewley & Dopita (2018) must be used. Bian, Kewley & Dopita (2018) selected a sample of local galaxies from the MPA-JHU value-added catalogue of SDSS DR7<sup>1</sup> (Abazajian et al. 2009) that are analogous to  $z \sim 2$  SF galaxies on the O3 versus [N II]6584/H $\alpha$  BPT diagram, making these calibrations more applicable to high-redshift samples. Bian, Kewley & Dopita (2018) used definitions of SF on the BPT diagram as defined in Kewley et al. (2013) for the local reference sample and Steidel et al. (2014) for the high- $z$  analogue sample (using Kewley et al. 2006 criterion to remove AGN and shock contamination to the emission line flux). The Bian, Kewley & Dopita (2018) calibrations used for our sample are

$$m = 8.54 - (0.59 \times \text{O32}_B), \quad (3)$$

$$\text{O3}_B = 43.9836 - 21.6211m + 3.4277m^2 - 0.1747m^3, \quad (4)$$

$$R_{23} = 138.0430 - 54.8284m + 7.2954m^2 - 0.32293m^3, \quad (5)$$

where  $\text{O32}_B = \log_{10}([\text{O III}]4959, 5007/[\text{O II}]3727, 3729)$ ,  $\text{O3}_B = \log_{10}([\text{O III}]4959, 5007/\text{H}\beta)$  and  $m = 12 + \log_{10}(\text{O}/\text{H})$ . We determined gas-phase metallicity values following the  $\chi^2$  minimization method explained in Section 4.1, including the same selection process for when [O II]3727 and/or H $\beta$  are poorly detected (an upper limit on [O II]3727, 3729 is used in Equation (3) in the case of both [O II]3727 and H $\beta$  being poorly detected, resulting in an upper limit on metallicity in all four cases where this was used). The solution to Equation (3) was used to discriminate between any multiple solutions. Equation (3) is suitable for  $0.3 < \text{O32} < 1.2$  (Bian, Kewley & Dopita 2018) but here, following the method of Li et al. (2023), we extrapolated the relationship linearly.

## 5 RESULTS

### 5.1 Mass-metallicity relation

Fig. 5 shows the MZR of our complete sample compared with other observational works. The left panel shows the MZR for our sample of J14-MEx SF galaxies, and the right panel shows the same but for our sample of C-MEx SF galaxies. The MZR was determined by measuring the best fit of the median stellar mass and gas-phase metallicity values in approximately equal-sized mass bins for both of our samples (8–9 SF galaxies per bin for the J14-MEx sample, and 12 SF galaxies per bin for the C-MEx sample). The error bars on these bins are the width of the bin in mass and the standard error for the median metallicity. These fits are compared with other works. The best fit was found to be linear in the form  $a \cdot x + b$ , where  $x = \log_{10}(M_*/M_\odot)$ ,  $a$  is the slope of the fit and  $b$  is the intercept.

<sup>1</sup><https://wwwmpa.mpa-garching.mpg.de/SDSS/DR7/>



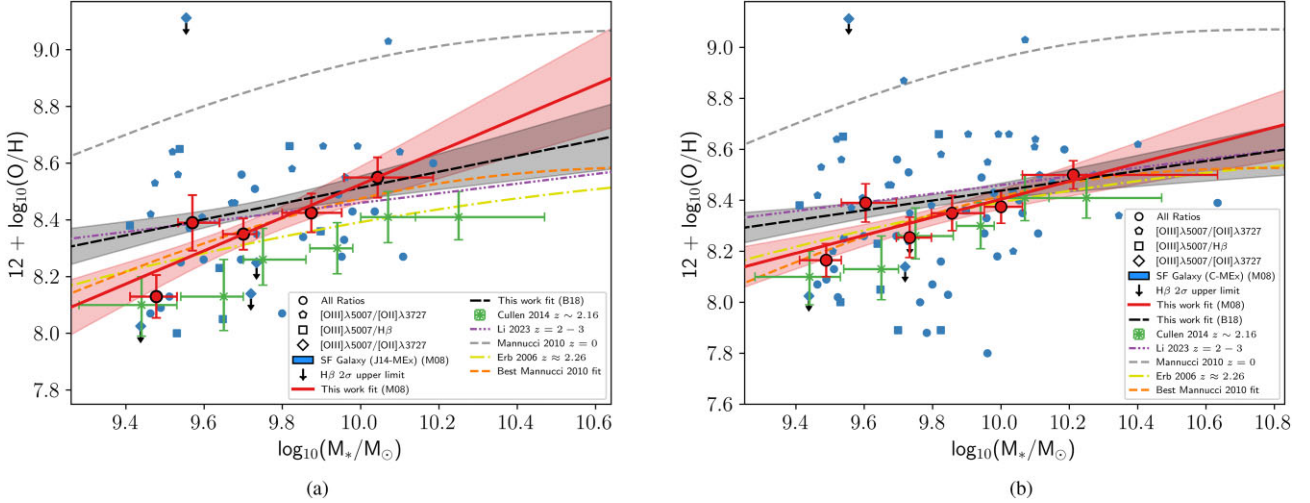


**Figure 5.** The MZR for our sample. The shape of the blue points (individual SF galaxies calibrated from the Maiolino et al. 2008 calibrations) are selected based on the strong-line ratio used to determine the galaxy’s gas-phase metallicity. Black arrows indicate limits on metallicity. The red circles are the binned averages of the SF galaxies within the completeness limit of our sample (8–9 SF galaxies per bin for the J14-MEx sample, and 12 SF galaxies per bin in the C-MEx sample), with the error on  $\log_{10}(M_*/M_\odot)$  representing the width of the bin, and error on metallicity being the standard error within that bin. The solid red line shows the fit of the binned averages of our Maiolino et al. (2008) sample (the red-shaded region indicates the  $1\sigma$  error of the fit). The green crosses show the Cullen et al. (2014) MZR data. The grey-dashed line shows the  $z = 0$  MZR from Mannucci et al. (2010), and the orange-dashed line shows the offset version of their best fit fitted to our sample. The yellow dash-dot line shows the MZR from Erb et al. (2006), which is the local Tremonti et al. (2004) MZR shifted by  $-0.56$  dex in metallicity to more closely match their  $z \approx 2.26$  sample. The purple dash-double dot line shows the linear MZR from Li et al. (2023). Erb et al. (2006) and Li et al. (2023) used different metallicity calibrations to those of our sample and direct comparisons should be noted with caution. The black-dashed line shows the best fit to median bins of our sample of SF galaxies when calibrated using the Bian, Kewley & Dopita (2018) metallicity calibrations, which are more applicable to high- $z$  (the black-shaded region indicates the  $1\sigma$  scatter of this fit). We do not plot the individual or binned data points of SF galaxies from the Bian, Kewley & Dopita (2018) calibrations to avoid confusion for the reader. As with the Erb et al. (2006) and Li et al. (2023) lines, this fit should be noted with caution.

**Table 2.** MZR fits for the binned data in Fig. 5 in the form  $12 + \log_{10}(\text{O}/\text{H}) = a \cdot \log_{10}(M_*/M_\odot) + b$ .

Maiolino et al. (2008) calibration	$a$	$b$
J14-MEx	$0.59 \pm 0.20$	$2.67 \pm 1.80$
C-MEx	$0.35 \pm 0.10$	$4.87 \pm 1.30$
Bian, Kewley & Dopita (2018) calibration	$a$	$b$
J14-MEx	$0.28 \pm 0.10$	$5.71 \pm 1.00$
C-MEx	$0.19 \pm 0.10$	$6.50 \pm 0.90$

The fit to our sample is shown by the red-dashed line in Fig. 5, with the red-shaded region representing the  $1\sigma$  scatter. The properties of these fits to both our J14-MEx and C-MEx samples can be found in Table 2. From both panels in Fig. 5, it can be seen that there is a correlation between gas-phase metallicity and stellar mass for the galaxies in our complete sample. The binned medians of our sample in the mass range of Cullen et al. (2014) ( $\log_{10}(M_*/M_\odot) = 9.44\text{--}10.25$ ) follow the same general trend, but their points are offset by  $-0.08 \pm 0.05$  dex in metallicity in the same mass range for our C-MEx sample ( $-0.17 \pm 0.06$  dex for our J14-MEx sample).

In order to compare our MZR to those of other studies, different forms of the MZR found by these works are fit to our data by allowing their intercept to vary but keeping higher order coefficients fixed. Doing this gives a clearer perspective on how the MZR found in this paper is different to those found in the literature. From the Mannucci et al. (2010) MZR, the best fit of their curve to our sample is offset from the original by  $-0.51 \pm 0.03$  dex in metallicity. This is a similar offset that is suggested by Erb et al. (2006) of  $-0.56$  dex from the

local Tremonti et al. (2004) MZR. This large offset is likely due to the fact Mannucci et al. (2010) based their MZR on a sample of local galaxies from SDSS which do not reflect the SF population of  $z \sim 2.2$  galaxies from our sample. It should be noted that comparisons between Mannucci et al. (2010) and Erb et al. (2006) should be made with caution because Erb et al. (2006) use the Pettini & Pagel (2004) metallicity calibrations whereas Mannucci et al. (2010) use those from Maiolino et al. (2008).

There is better agreement between the Li et al. (2023) MZR and our data, with just a small average offset from their MZR to ours of  $\approx -0.04$  dex in metallicity for our C-MEx sample ( $\approx -0.08$  dex offset for the J14-MEx sample). This consistency should be noted with caution as Li et al. (2023) use metallicity calibrations from Bian, Kewley & Dopita (2018) whereas the comparisons above are using results calibrated using Maiolino et al. (2008). In order to make a more accurate comparison to Li et al. (2023), we have overlaid the MZR derived from the Bian, Kewley & Dopita (2018) for the same samples of galaxies (black-dashed line in Fig. 5). We find the MZR exists at  $z \sim 2.2$  with these higher redshift calibrations, albeit with a shallower slope for both the J14-MEx and C-MEx sample (see Table 2). The difference from the Li et al. (2023) MZR is just  $\approx -0.03$  dex in metallicity for the C-MEx sample ( $\approx 0.04$  dex offset for the J14-MEx sample). These offsets are similar and the slopes are much more consistent; the Li et al. (2023) MZR occupies the  $1\sigma$  scatter of our fit for almost the entire mass range of our C-MEx sample.

In Fig. 6, we compare the MZR of our C-MEx sample using both the Maiolino et al. (2008) (dashed red line) and Bian, Kewley & Dopita (2018) (black-dashed line) calibrations to results from simulations in the literature at comparable redshifts. These simulations



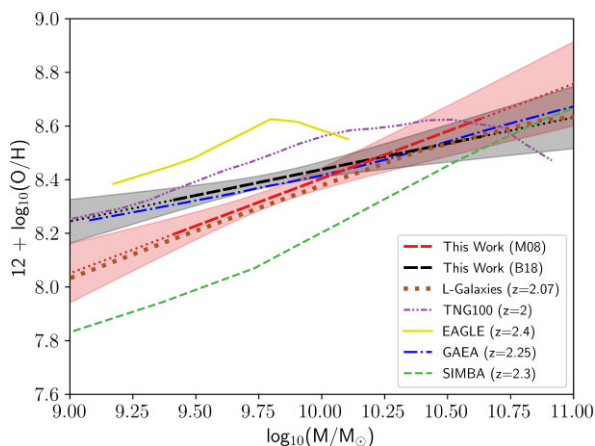


**Figure 6.** The MZR for our sample compared to MZRs generated from simulations of galaxy evolution. The dashed red line shows the fit of the binned averages of our C-MEx sample using metallicity calibrations from Maiolino et al. (2008) (the red-shaded region indicates the  $1\sigma$  error of the fit). The dashed black line shows the fit of the binned averages of our C-MEx sample using metallicity calibrations from Bian, Kewley & Dopita (2018) (the black-shaded region indicates the  $1\sigma$  error of the fit). The brown dotted line indicates the  $z = 2.07$  binned median MZR relationship of the cosmological semi-analytic galaxy evolution simulation, L-Galaxies from Yates et al. (2023). The dash-dotted purple line shows the  $z = 2$  MZR derived from the IllustrisTNG TNG100 cosmological hydrodynamical simulation in Torrey et al. (2019). The solid yellow line shows the  $z = 2.4$  MZR determined by De Rossi et al. (2017) using the EAGLE suite of cosmological hydrodynamical simulations. The blue dash-dotted shows the shifted  $z = 2.25$  MZR from analysis by Fontanot et al. (2021) using the GAEA semi-analytical model of galaxy formation. The green-dashed line indicates the Davé et al. (2019)  $z = 2.3$  MZR using the SIMBA cosmological hydrodynamical simulations.

are the  $z = 2.07$  binned median MZR from L-Galaxies<sup>2</sup> in Yates et al. (2023), which is a cosmological semi-analytic galaxy evolution simulation (Springel et al. 2005; Henriques et al. 2020); the  $z = 2$  MZR found by Torrey et al. (2019), derived from the IllustrisTNG TNG100 cosmological hydrodynamical simulation (Marinacci et al. 2018); the  $z = 2.4$  MZR determined by De Rossi et al. (2017) using the Evolution and Assembly of GaLaxies and their Environments (EAGLE) suite of cosmological hydrodynamical simulations; the  $z = 2.25$  MZR from analysis by Fontanot et al. (2021) using the GAEA semi-analytical model of galaxy formation (Hirschmann, De Lucia & Fontanot 2016); and the  $z = 2.3$  MZR from Davé et al. (2019) found using the SIMBA cosmological hydrodynamical simulations. For the Fontanot et al. (2021) line, we chose to use their MZR that is shifted by  $-0.1$  dex in metallicity from their intrinsic model predictions. We selected this instead of the direct model because, as Fontanot et al. (2021) explain, this shift is acceptable given the uncertainty in the normalization of the MZR from the metallicity indicators, and this offset finds much better agreement with the  $z \sim 0$  observations they compare to, whilst maintaining agreement with observations at all other redshifts they analyse (see their Section 4.1). From Fig. 6, the MZR of our C-MEx galaxies for both calibrations generally agree with those measured in simulations at these redshifts, especially at higher masses ( $\sim 10^{10.25}$ – $10^{10.75} M_\odot$ ), although the EAGLE simulations from De Rossi et al. (2017) only go up to  $\sim 10^{10.1} M_\odot$ . The MZR from L-Galaxies (Yates et al. 2023), which is the median binned relationship of their simulated galaxies,

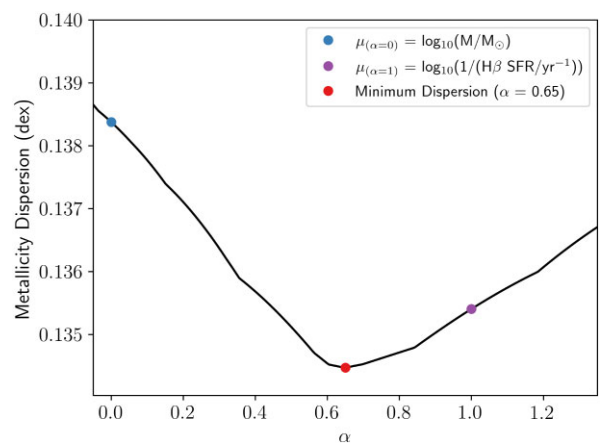


**Figure 7.** Metallicity dispersion of SF galaxies defined using the C-MEx as a function of  $\alpha$  (defined in equation 6). Shown are  $\alpha$  values corresponding to the minimum dispersion about metallicity ( $\alpha = 0.69$ , red point),  $\alpha = 0$  ( $\mu_0 = \log_{10}(M_*/M_\odot)$ , blue point) and  $\alpha = 1$  ( $\mu_1 = \log_{10}(1/(H\beta \text{ SFR}/\text{yr}^{-1}))$ , purple point).

agrees remarkably well with our Maiolino et al. (2008) calibrated relationship at low stellar masses ( $\sim 10^9$ – $10^{10} M_\odot$ ), but then strongly agrees with our Bian, Kewley & Dopita (2018) calibrated relationship at higher stellar masses ( $\sim 10^{10.25}$ – $10^{11} M_\odot$ ) following a flattening of their relationship. Additionally, there is strong agreement between the semi-analytic model from Fontanot et al. (2021) and our Bian, Kewley & Dopita (2018) calibrated sample for the entire mass range of Fig. 6, with their MZR not falling outside the  $1\sigma$  scatter of our relationship.

## 5.2 The Fundamental Metallicity Relation

Mannucci et al. (2010) introduced a way to project the 3D relationship between SFR, stellar mass and gas-phase metallicity onto a 2D plane by combining stellar mass and SFR into a single axis. They describe that this should show a more accurate correlation with gas-phase metallicity because, for a given stellar mass, galaxies with a higher SFR have reduced metallicities and exhibit properties of lower mass galaxies. As a result, while direct relationships between SFR and gas-phase metallicity may show that they are directly correlated properties, they may be masking over more complicated trends when stellar mass is considered as well. This FMR projection is in the form

$$\mu_\alpha = \log_{10}(M_*/M_\odot) - \alpha \log_{10}(\text{SFR}/M_\odot \text{yr}^{-1}), \quad (6)$$

where  $\alpha$  is a free parameter determined by finding the minimum gas-phase metallicity dispersion in this plane. For their data, Mannucci et al. (2010) found  $\alpha = 0.32$ . For our samples, using the higher redshift metallicity calibrations from Bian, Kewley & Dopita (2018), the scatter around metallicity was minimized for  $\alpha = 0.48$  when using the J14-MEx, and  $\alpha = 0.65$  for the C-MEx sample. The latter value of 0.65 is consistent with  $\alpha$  values obtained for galaxies in this redshift range in the literature (e.g. Curti et al. 2020a; Sanders et al. 2021; and Li et al. 2023, see below). Fig. 7 shows the metallicity dispersion as a function of  $\alpha$  for the C-MEx sample. Despite still indicating the existence of an FMR, an  $\alpha$  of 0.48 for the J14-MEx sample is somewhat at odds with expected values at this redshift range. Randomly sampling the C-MEx sample to match the size of the J14-MEx sample 10 000 times gives an average  $\alpha \approx 0.71 \pm 0.19$ , which is consistent with the C-MEx value of  $\alpha = 0.65$ . This suggests

<sup>2</sup><https://lgalaxiespublicrelease.github.io>

that the smaller sample size resulting from the more restrictive J14-MEx prescriptions is not the primary cause of the lower value. The lower  $\alpha$  is instead likely due to the J14-MEx samples not probing as wide a mass and SFR range as the C-MEx sample. Fig. 8 shows the FMR using these obtained  $\alpha$  values for our [O III]5007 flux and stellar mass complete sample. The FMR in Fig. 8(b), which is for our C-MEx sample, is constructed in the form of

$$12 + \log_{10}(\text{O}/\text{H}) = (4.8 \pm 0.9) + (0.4 \pm 0.1)\mu_{0.65}. \quad (7)$$

This linear form is fit to equally sized bins of our complete sample showing the median metallicity of the galaxies in each bin. The significance of the slope of this relation is  $\sim 4\sigma$ , calculated by dividing the slope of the fit by its uncertainty. The shaded region around the red-dashed line indicates the  $1\sigma$  uncertainty about the fit.

Comparisons with the FMRs of other works can be done by using their values of  $\alpha$ , making sure to maintain the same calibrations for metallicity calculations. Fig. 9 shows our samples on the FMR plane of Mannucci et al. (2010), with the purple fit showing their general form of the FMR for galaxies of any stellar mass, SFR and redshift up to  $z \approx 2.5$ . We used the metallicity calibrations from Maiolino et al. (2008) for this comparison. The Mannucci et al. (2010) FMR is in the form

$$12 + \log_{10}(\text{O}/\text{H}) = \begin{cases} 8.90 + 0.47(\mu_{0.32} - 10) & \text{if } \mu_{0.32} < 10.2 \\ 9.07 & \text{if } \mu_{0.32} > 10.5. \end{cases} \quad (8)$$

All the galaxies in our sample have  $\mu_{0.32} < 10.2$ , so for simplicity, we will represent this as  $12 + \log_{10}(\text{O}/\text{H}) = 4.20 + 0.47\mu_{0.32}$ . From Fig. 9(b), using  $\alpha = 0.32$  and  $x = \mu_{0.32}$ , the FMR for our sample of C-MEx SF galaxies is found to be

$$12 + \log_{10}(\text{O}/\text{H}) = (3.92 \pm 1.0) + (0.47 \pm 0.10)\mu_{0.32}. \quad (9)$$

The slope is in very good agreement with the general linear form found by Mannucci et al. (2010), but is offset by  $\sim 0.28 \pm 0.04$  dex in metallicity in the  $\mu_{0.32}$  range of the sample. The error on this offset is the median  $1\sigma$  error about our fit in this range. This offset is in good agreement with Cullen et al. (2014), who found that the FMR of their sample of  $z_{\text{median}} \sim 2.16$  SF galaxies, also observed with *HST* grism, was offset by an average of  $\sim 0.3$  dex. They determined that this discrepancy is due to the selection of metallicity indicator because Maiolino et al. (2008) rely on local SF galaxies to determine their metallicity calibrations, which may not be applicable at high- $z$ , and our result adds evidence to this suggestion.

Fig. 10 shows the FMR found by Li et al. (2023) for  $z = 2-3$  dwarf galaxies (brown dash-double dot line). Using their value of  $\alpha = 0.6$  for the galaxies in our C-MEx sample, and using the Bian, Kewley & Dopita (2018) metallicity calibrations as they do, yields an FMR in the form

$$12 + \log_{10}(\text{O}/\text{H}) = (4.76 \pm 0.9) + (0.40 \pm 0.1)\mu_{0.60}. \quad (10)$$

This form is a much steeper slope than the trend found by Li et al. (2023) of  $(0.17 \pm 0.02)\mu_{0.60}$ . This could be caused by the contributions of their lower mass bins ( $\sim 10^{6.5} - 10^{7.6} M_{\odot}$ ) which extend beyond the lower limit of masses in this work. Instead, a more appropriate comparison would be to the  $z \sim 2.3$  Sanders et al. (2021) sample (pink triangles) in Fig. 10 as they all fall within the  $\mu_{0.60}$  range of this work (red points) and were also used for comparison in Li et al. (2023). Sanders et al. (2021) investigated the redshift evolution of the MZR by analysing samples of galaxies at  $z \sim 2.3$  and 3.3 from the MOSFIRE Deep Evolution Field Survey (see Kriek et al. 2015). Comparisons are made to their  $z \sim 2.3$  sample as it is a similar redshift to the galaxies in our complete sample and they use

the metallicity calibrations from Bian, Kewley & Dopita (2018). A fit to their sample in the same form as the FMR from Li et al. (2023) yields

$$12 + \log_{10}(\text{O}/\text{H}) = (4.39 \pm 0.4) + (0.45 \pm 0.04)\mu_{0.60}, \quad (11)$$

which is in good agreement with our work. This is more evidence that the FMR exists for SF galaxies at this redshift.

Li et al. (2023) discuss the possible reasons why their slope of the MZR is shallower than that of Sanders et al. (2021). They suggest that the evolution of the MZR slope may be determined by different feedback mechanisms and wind models, both of which regulate the fraction of gas ejected from a galaxy (Wang et al. 2022) and determine the MZR in individual galaxies. If low-mass galaxies are dominated by different feedback mechanisms compared to high-mass galaxies, then an evolution in the MZR will be visible. They comment that the results of their study are consistent with that of a momentum-driven wind model (see Finlator & Davé 2008; Guo et al. 2016) but at odds with other studies that analyse the MZR at low mass (e.g. Torrey et al. 2019). Given our FMR results agree with Sanders et al. (2021) for an overlapping  $\mu_{0.60}$  range, but see a steepening of the slope compared to the lower range of Li et al. (2023), it seems to suggest that there is a turnover in these relationships from low to high mass at  $z \sim 2.2$ . However, while the reasons above for a steepening of the slope in the MZR could apply to a change in slope in the FMR toward higher  $\mu_{\alpha}$  values, Li et al. (2023) highlight the need for further analysis of the MZR in dwarf galaxies at these redshifts before making any firm conclusions. Additionally, the fact our Bian, Kewley & Dopita (2018) MZR slopes agree with Li et al. (2023) indicates that the above explanations regarding different wind models should not be confidently applied to the FMR.

## 6 DISCUSSION AND CONCLUSIONS

This work analyses the relationship between gas-phase metallicity, stellar mass and SFR in  $z = 1.99-2.32$  SF galaxies from QSAGE. We used the commonly used [O II]3727,3729, [O III]4958,5007 and H $\beta$  strong-emission lines in order to calibrate metallicities (Maiolino et al. 2008; Bian, Kewley & Dopita 2018) as they lie in the wavelength range of *HST* grism spectra at these redshifts. Since many strong-emission lines that are used to generate BPT diagrams (Baldwin, Phillips & Terlevich 1981) are unavailable in the wavelength range of our grism spectra, MEx diagrams from Juneau et al. (2014) and Coil et al. (2015) were used to differentiate SF galaxies from AGN. These MEx diagrams use the O3 strong-emission line ratio. As a result of the nature of the observations, [O III]5007 flux and stellar mass limits were applied in order to negate selection effects that arise from incomplete bins in these two properties. SF galaxies were binned in equal-sized mass bins and an MZR was constructed and compared to previous works in the literature, including MZRs constructed using  $z \sim 0$  galaxies. In the analysis of the FMR, SF galaxies are binned in equal sized  $\mu_{\alpha}$  bins (see Equation 6), where  $\alpha$  varies depending the scatter in gas-phase metallicity. The conclusions of this work are as follows:

- i) Using the metallicity calibrations from Maiolino et al. (2008) – making use of four different strong-emission line ratios in our available wavelength range – an MZR can be seen for SF galaxies at the redshift range of our sample. MZRs were built using both of the two MEx diagnostics from Juneau et al. (2014) and Coil et al. (2015) using measured values and upper limits for H $\beta$  flux in the MEx plane. In both of the SF galaxy samples (Fig. 5), the MZR

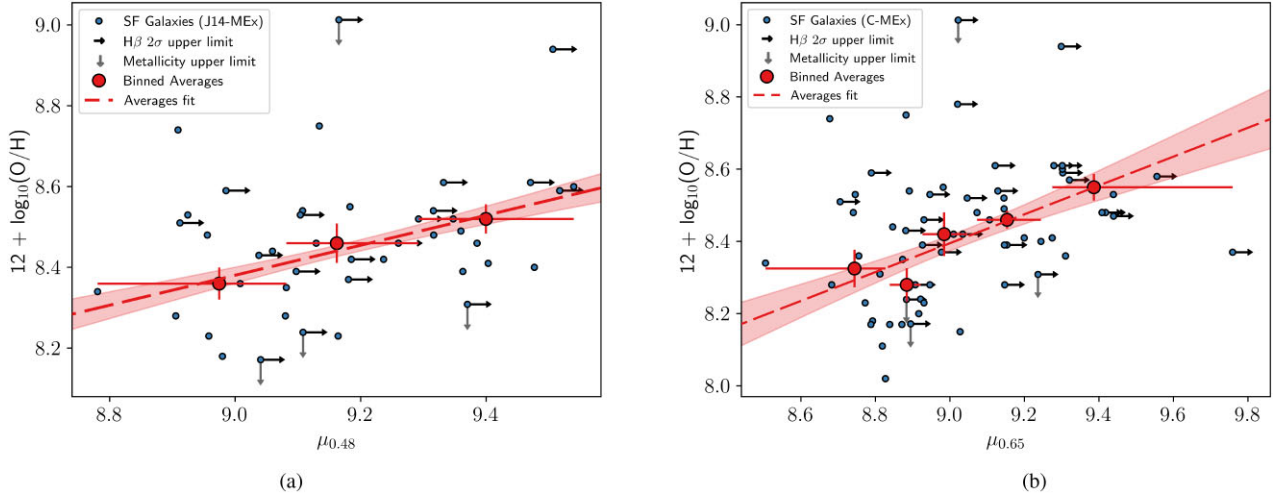


**Figure 8.** The 2D projection of the FMR using the form  $\mu_\alpha = \log_{10}(M) - \alpha \log_{10}(\text{SFR})$  as introduced in Mannucci et al. (2010). The  $\alpha$  values in both panels are those calculated when the scatter about gas-phase metallicity is minimized. Left panel: the 2D-projected FMR using SF galaxies as defined by the shifted J14-MEx curve, where  $\alpha = 0.48$ . Right panel: the 2D-projected FMR using SF galaxies as defined by the C-MEx, where  $\alpha = 0.65$ . In both panels, the blue points show the individual SF galaxies in our complete sample. The red points show the median values for our complete sample in approximately equal sized  $\mu_\alpha$  bins, with the red-dashed line showing the best fit to these points (the red-shaded regions indicate the  $1\sigma$  scatter about the fit).

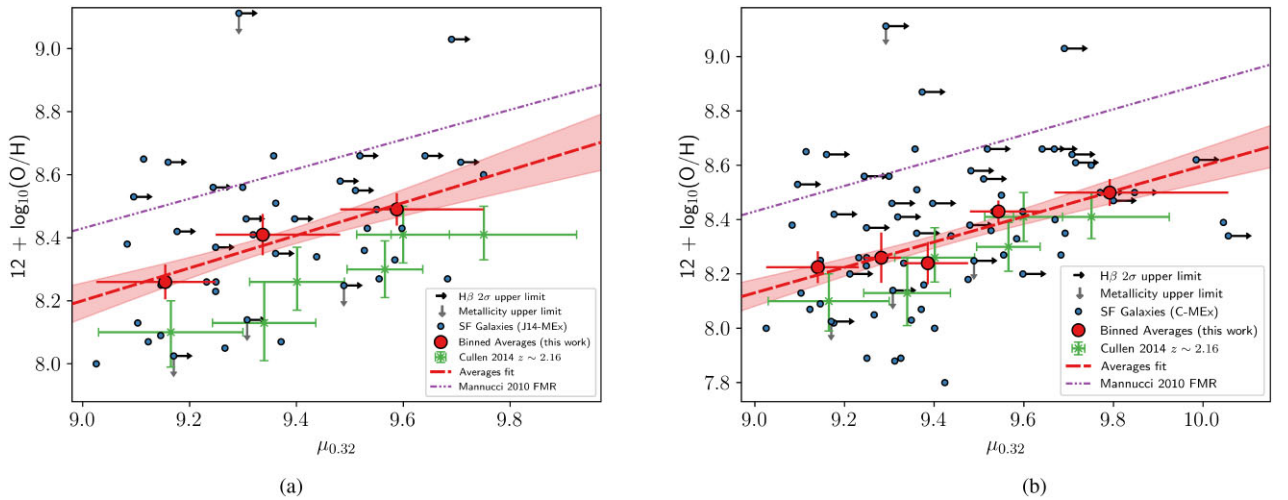


**Figure 9.** The 2D projection of the FMR using the form  $\mu_{0.32} = \log_{10}(M) - 0.32 \log_{10}(\text{SFR}) - 10$  as used by Mannucci et al. (2010).  $\alpha = 0.32$  was found to minimize the scatter on gas-phase metallicity of local SDSS galaxies by Mannucci et al. (2010). Left panel: the 2D-projected FMR using SF galaxies from our sample as defined by the shifted J14-MEx. Right panel: The 2D-projected FMR using SF galaxies from our sample as defined by the C-MEx. In both panels, the purple dash-double-dot line shows the exact form found by Mannucci et al. (2010) for galaxies of all stellar mass, SFR and at any redshift when  $\mu_{0.32} < 10.2$ . The blue points show the individual SF galaxies within our complete sample. The red points show the median values for SF galaxies in our complete sample in equal-sized  $\mu_{0.32} - 10$  bins, with the red-dashed line showing the best fit to these points (the red-shaded region indicates the  $1\sigma$  scatter about the fit). The green crosses show the data from Cullen et al. (2014) in this plane.

constructed from this work is consistent with MZR in the literature for similar redshift ranges (Erb et al. 2006; Cullen et al. 2014).

ii) We compared the MZR of our C-MEx sample to a variety of cosmological hydrodynamical simulations and semi-analytic models at comparable redshifts ( $z = 2-2.4$ ), using both the Maiolino et al. (2008) and Bian, Kewley & Dopita (2018) metallicity calibrations. We find that, in general, these simulations are consistent with our MZR, particularly at higher stellar masses of  $\approx 10^{10.25} - 10^{10.75} M_\odot$ .

iii) The FMR was investigated using a 2D projection that combines stellar mass and SFR (see Mannucci et al. 2010). Analysis using  $\alpha = 0.65$ , a value which minimizes the dispersion about gas-phase metallicity for C-MEx galaxies, yields an  $\sim 4\sigma$  slope for the best fit

in this FMR plane. This value of  $\alpha$  agrees broadly with recent values in the literature at this redshift. Using the J14-MEx, the value for  $\alpha$  which minimizes dispersion around gas-phase metallicity comes to  $\alpha = 0.48$ . Despite not agreeing with  $\alpha$  values at this redshift in the literature, this fit is still consistent with an FMR being present in our sample. The lower value of  $\alpha$  could be due to the J14-MEx not probing as wide a stellar mass and SFR range.

iv) In the Mannucci et al. (2010) FMR plane, where  $\alpha = 0.32$ , our results show that the FMR exists for both J14-MEx and C-MEx diagnostics (Fig. 9). Using the C-MEx, the slope for our sample came to  $0.47 \pm 0.08$ , a value that is in excellent agreement for the SDSS sample in Mannucci et al. (2010). The FMR is offset by



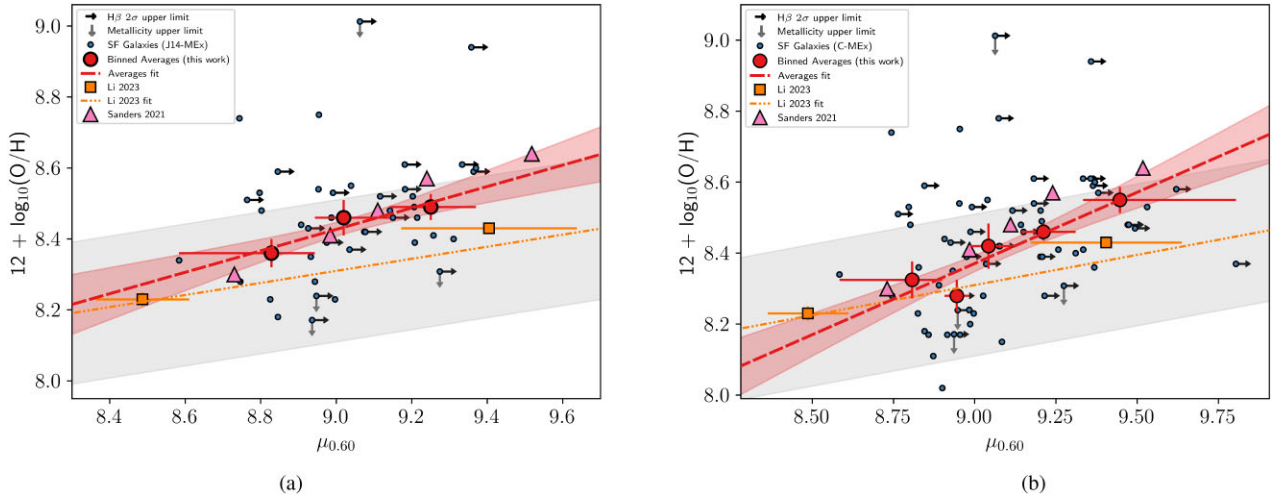


**Figure 10.** The 2D projection of the FMR using the form  $\mu_{0.60} = \log_{10}(M) - 0.60\log_{10}(\text{SFR})$  as used by Li et al. (2023).  $\alpha = 0.60$  was found to minimize the scatter on gas-phase metallicity of the  $z = 2-3$  galaxies in Li et al. (2023). Left panel: the 2D-projected FMR using SF galaxies from our sample as defined by the shifted J14-MEx. Right panel: the 2D-projected FMR using SF galaxies from our sample as defined by the C-MEx. In both panels, the orange squares show the median values from Li et al. (2023) as defined in their paper, with the orange dash-double-dot line showing their fit (grey-shaded region indicates the  $1\sigma$  scatter about their fit). The pink triangles show the median values of data from Sanders et al. (2021) in this plane. The blue points show the individual SF galaxies in our complete sample. The red points show the median values in equal-sized  $\mu_{0.60}$  bins for our complete sample, with the red-dashed line showing the best fit to these points (the red-shaded region indicates the  $1\sigma$  scatter about our fit).

$0.28 \pm 0.04$  dex in metallicity, which is consistent with the offset found by Cullen et al. (2014). According to Mannucci et al. (2010), this FMR should be consistent for all stellar masses, SFRs, and redshifts so this offset could be a result of the choice of metallicity calibration at this redshift, a conclusion Cullen et al. (2014) (who similarly used the Maiolino et al. 2008 calibrations) came to.

v) Using  $\alpha = 0.6$  as was used by Li et al. (2023), the FMR is again found for both J14-MEx and C-MEx SF galaxies. For C-MEx galaxies, the slope of the FMR is found to be  $0.40 \pm 0.1$ . This is similar to the slope in the Mannucci et al. (2010) plane but much steeper than the slope found by Li et al. (2023). This is likely due to the fact their stellar mass range extends down by an additional  $\sim 3$  dex compared to our sample. The slope is in very good agreement with a fitted slope to the Sanders et al. (2021) data in the same plane ( $0.45 \pm 0.04$ ), who had a  $\mu_{0.60}$  range that overlapped completely with that of this work. The FMR being visible in all three planes analysed in this work strongly suggests that it exists in SF galaxies at this redshift.

Regarding the FMR, we believe the negative correlation with SFR at fixed mass is due to the accretion of metal-poor gas fuelling SFR at cosmic noon (e.g. Kereš et al. 2005; Dekel, Sari & Ceverino 2009). There is mounting evidence in the literature that metallicity gradients of higher sSFR galaxies are flat or even positive (i.e. lower metallicity in the central region and increasing with radius; Stott et al. 2014. See also Wang et al. 2017; Gillman et al. 2020, 2022). It is believed these positive metallicity gradients are caused by this metal-poor gas accretion being focussed on the centre of the galaxy (Sharda et al. 2021) which can be triggered by either efficient accretion (Stott et al. 2014) or merger events (Rupke, Kewley & Barnes 2010). Accretion of low-metallicity gas like this results in a dilution of the chemical-abundance. Recently, Heintz et al. (2023) used public *JWST* Near-Infrared Spectrograph data sets to analyse  $z > 7$  galaxies, and suggested that the drop in gas-phase metallicity they see in these very high redshift galaxies is a result of dilution caused by accretion. Funnelled accretion then drives high sSFR in

the centre of galaxies and is thought to be the cause of a relationship between sSFR and metallicity gradient (Wuyts et al. 2016; Curti et al. 2020b). In this context, metal-poor gas being efficiently accreted into the central cores of the galaxies greatly enhances the SFR whilst simultaneously reducing the overall average gas-phase metallicity of a galaxy on short time-scales, which drives the negative correlation between SFR and gas-phase metallicity for fixed stellar mass we see in the FMR (see also Troncoso et al. 2014; Kashino et al. 2017; Wang et al. 2019; Simons et al. 2021). Results from simulations of galaxy evolution lend support to this. From analysis of galaxies in the EAGLE simulations, De Rossi et al. (2017) found that for lower mass galaxies ( $M_* < 10^{10.3} M_\odot$ ), their results indicate higher fractions of metal-poor gas drive higher sSFRs and reduce gas-phase metallicity values, and that this is regulated by metal-poor inflows, with a particular focus on satellite galaxies. It is worth noting that for their higher mass systems ( $M_* \gtrsim 10^{10.3} M_\odot$ ), the impact of AGN feedback becomes much more significant to the point where it causes an inversion in the MZR plane for fixed stellar mass; metallicity starts increasing with sSFR for fixed stellar masses at  $\gtrsim 10.3 M_\odot$ , but at lower masses it is an anticorrelation at fixed stellar mass (they also found a similar inversion at fixed stellar mass for the gas fraction of the SF component of gas). Torrey et al. (2019) found that accretion plays a significant role shaping the FMR in SF galaxies in TNG100, and that, additionally, the MZR is a consequence of the accretion (and enrichment) history of galaxies.

## ACKNOWLEDGEMENTS

The authors gratefully acknowledge the significant contribution to this project made by the late Richard G. Bower. His scientific expertise and enthusiasm are sorely missed. The authors thank the anonymous referee for their helpful comments that have increased the clarity of this work. HMOS gratefully acknowledges support from an STFC PhD studentship and the Faculty of Science and Technology at Lancaster University. MF and RD would like to acknowledge funding from the European Research Council (ERC) under the European

Union’s Horizon 2020 research and innovation programme (grant agreement no 757535). For the purpose of open access, the authors have applied creative commons attribution (CC BY) licence to any author accepted manuscript version arising.

## DATA AVAILABILITY

The data underlying this article are from *HST* Cycle 24 proposal 14594: ‘QSAGE: QSO Sightline And Galaxy Evolution’ and are publicly available from the Mikulski Archive for Space Telescopes (MAST, <https://archive.stsci.edu/hst/>).

## REFERENCES

- Abazajian K. N. et al., 2009, *ApJS*, 182, 543
- Adelman-McCarthy J. K. et al., 2006, *ApJS*, 162, 38
- Andrews B. H., Martini P., 2013, *ApJ*, 765, 140
- Baker W. M., Maiolino R., 2023, *MNRAS*, 521, 4173
- Baker W. M. et al., 2022, *MNRAS*, 519, 1149
- Baldwin J. A., Phillips M. M., Terlevich R., 1981, *Publ. Astron. Soc. Pac.*, 93, 5
- Barrera-Ballesteros J. K., Sánchez S. F., Heckman T., Blanc G. A., The MaNGA Team, 2017, *ApJ*, 844, 80
- Barro G. et al., 2019, *ApJS*, 243, 22
- Bian F., Kewley L. J., Dopita M. A., 2018, *ApJ*, 859, 175
- Bielby R., Crighton N. H. M., Fumagalli M., Morris S. L., Stott J. P., Tejos N., Cantalupo S., 2017, *MNRAS*, 468, 1373
- Bielby R. M. et al., 2019, *MNRAS*, 486, 21
- Bothwell M. S., Maiolino R., Kennicutt R., Cresci G., Mannucci F., Marconi A., Ciccone C., 2013, *MNRAS*, 433, 1425
- Brammer G., 2019, Astrophysics Source Code Library, record ascl:1905.001
- Brammer G. B. et al., 2012, *ApJS*, 200, 13
- Bresolin F., 2007, *ApJ*, 656, 186
- Brown T., Cortese L., Catinella B., Kilborn V., 2018, *MNRAS*, 473, 1868
- Bruzual G., Charlot S., 2003, *MNRAS*, 344, 1000
- Bundy K. et al., 2014, *ApJ*, 798, 7
- Chabrier G., 2003, *Publ. Astron. Soc. Pac.*, 115, 763
- Charlot S., Longhetti M., 2001, *MNRAS*, 323, 887
- Coil A. L. et al., 2015, *ApJ*, 801, 35
- Colbert J. W. et al., 2013, *ApJ*, 779, 34
- Collacchioni F., Cora S. A., Lagos C. D. P., Vega-Martínez C. A., 2018, *MNRAS*, 481, 954
- Cresci G., Mannucci F., Curti M., 2019, *A&A*, 627, A42
- Cullen F., Cirasuolo M., McLure R. J., Dunlop J. S., Bowler R. A. A., 2014, *MNRAS*, 440, 2300
- Cullen F. et al., 2019, *MNRAS*, 487, 2038
- Cullen F. et al., 2021, *MNRAS*, 505, 903
- Curti M., Mannucci F., Cresci G., Maiolino R., 2020a, *MNRAS*, 491, 944
- Curti M. et al., 2020b, *MNRAS*, 492, 821
- Curti M. et al., 2022, *MNRAS*, 518, 425
- Curti M. et al., 2023, preprint (arXiv:2304.08516)
- Davé R., Finlator K., Oppenheimer B. D., Fardal M., Katz N., Kereš D., Weinberg D. H., 2010, *MNRAS*
- Davé R., Anglés-Alcázar D., Narayanan D., Li Q., Rafieferantsoa M. H., Appleby S., 2019, *MNRAS*, 486, 2827
- De Lucia G., Xie L., Fontanot F., Hirschmann M., 2020, *MNRAS*, 498, 3215
- De Rossi M. E., Bower R. G., Font A. S., Schaye J., Theuns T., 2017, *MNRAS*, 472, 3354
- Dekel A., Sari R., Ceverino D., 2009, *ApJ*, 703, 785
- Dopita M. A. et al., 2006, *ApJS*, 167, 177
- Dopita M. A., Kewley L. J., Sutherland R. S., Nicholls D. C., 2016, *Ap&SS*, 361, 61
- Dors Jr O. L., Krabbe A., Hägele G. F., Pérez-Montero E., 2011, *MNRAS*, 415, 3616
- Dutta R. et al., 2021, *MNRAS*, 508, 4573
- Edmunds M. G., 1990, *MNRAS*, 246, 678
- Ellison S. L., Patton D. R., Simard L., McConnachie A. W., 2008, *ApJ*, 672, L107
- Erb D. K., Shapley A. E., Pettini M., Steidel C. C., Reddy N. A., Adelberger K. L., 2006, *ApJ*, 644, 813
- Ferland G. J., Chatzikos M., Guzman F., Lykins M. L., Badnell N. R., Keenan F. P., Porter R. L., Stancil P. C., 2017, *Rev. Mex. Astron. Astrofis.*, 58, 385
- Finlator K., Davé R., 2008, *MNRAS*, 385, 2181
- Fontanot F. et al., 2021, *MNRAS*, 504, 4481
- Garg P. et al., 2022, *ApJ*, 926, 80
- Garg P., Narayanan D., Sanders R. L., Davé R., Popping G., Shapley A. E., Stark D. P., Trump J. R., 2023, preprint (arXiv:2310.08622)
- Garnett D. R., Shields G. A., 1987, *ApJ*, 317, 82
- Gaskell C. M., Ferland G. J., 1984, *Publ. Astron. Soc. Pac.*, 96, 393
- Gillman S. et al., 2020, *MNRAS*, 500, 4229
- Gillman S. et al., 2022, *MNRAS*, 512, 3480
- Guo Y. et al., 2016, *ApJ*, 822, 103
- Hayashi M. et al., 2020, *Publ. Astron. Soc. Japan*, 72, 86
- Heintz K. E. et al., 2023, *Nat. Astron.*
- Henriques B. M. B., Yates R. M., Fu J., Guo Q., Kauffmann G., Srisawat C., Thomas P. A., White S. D. M., 2020, *MNRAS*, 491, 5795
- Henry A. et al., 2013, *ApJ*, 776, L27
- Hirschmann M., De Lucia G., Fontanot F., 2016, *MNRAS*, 461, 1760
- Jimmy, Tran K.-V., Saintonge A., Accurso G., Brough S., Oliva-Altamirano P., 2015, *ApJ*, 812, 98
- Juneau S., Dickinson M., Alexander D. M., Salim S., 2011, *ApJ*, 736, 104
- Juneau S. et al., 2013, *ApJ*, 764, 176
- Juneau S. et al., 2014, *ApJ*, 788, 88
- Kashino D. et al., 2017, *ApJ*, 835, 88
- Kashino D. et al., 2022, *ApJ*, 925, 82
- Kauffmann G. et al., 2003, *MNRAS*, 341, 33
- Kennicutt R. C., 1998, *ARA&A*, 36, 189
- Kereš D., Katz N., Weinberg D. H., Dave R., 2005, *MNRAS*, 363, 2
- Kewley L. J., Dopita M. A., 2002, *ApJS*, 142, 35
- Kewley L. J., Ellison S. L., 2008, *ApJ*, 681, 1183
- Kewley L. J., Groves B., Kauffmann G., Heckman T., 2006, *MNRAS*, 372, 961
- Kewley L. J., Dopita M. A., Leitherer C., Davé R., Yuan T., Allen M., Groves B., Sutherland R., 2013, *ApJ*, 774, 100
- Kewley L. J., Nicholls D. C., Sutherland R. S., 2019, *ARA&A*, 57, 511
- Khostovan A. A., Sobral D., Mobasher B., Best P. N., Smail I., Stott J. P., Hemmati S., Nayyeri H., 2015, *MNRAS*, 452, 3948
- Kriek M. et al., 2015, *ApJS*, 218, 15
- Kroupa P., 2001, *MNRAS*, 322, 231
- Lagos P., Demarco R., Papaderos P., Telles E., Nigoche-Netro A., Humphrey A., Roche N., Gomes J. M., 2016, *MNRAS*, 456, 1549
- Langan I. et al., 2023, *MNRAS*, 521, 546
- Lara-López M. A. et al., 2010, *A&A*, 521, L53
- Lequeux J., Peimbert M., Rayo J. F., Serrano A., Torres-Peimbert S., 1979, *A&A*, 80, 155
- Li M. et al., 2023, *ApJ*, 955, L18
- van Loon M. L., Mitchell P. D., Schaye J., 2021, *MNRAS*, 504, 4817
- Ly C., Malkan M. A., Rigby J. R., Nagao T., 2016, *ApJ*, 828, 67
- Madau P., Dickinson M., 2014, *ARA&A*, 52, 415
- Maiolino R., Mannucci F., 2019, *A&AR*, 27, 3
- Maiolino R. et al., 2008, *A&A*, 488, 463
- Mannucci F. et al., 2009, *MNRAS*, 398, 1915
- Mannucci F., Cresci G., Maiolino R., Marconi A., Gnerucci A., 2010, *MNRAS*, 408, 2115
- Mannucci F., Salvaterra R., Campisi M. A., 2011, *MNRAS*, 414, 1263
- Marinacci F. et al., 2018, *MNRAS*
- Nagao T., Maiolino R., Marconi A., 2006, *A&A*, 459, 85
- Newman S. F. et al., 2013, *ApJ*, 781, 21
- Osterbrock D. E., Ferland G. J., 2006, *Astrophysics of Gaseous Nebulae and Active Galactic Nuclei*. Univ. Science Books, Sausalito, CA
- Pettini M., Pagel B. E. J., 2004, *MNRAS*, 348, L59
- Price S. H. et al., 2014, *ApJ*, 788, 86
- Rupke D. S. N., Kewley L. J., Barnes J. E., 2010, *ApJ*, 710, L156

- Sakstein J., Pipino A., Devriendt J. E. G., Maiolino R., 2011, *MNRAS*, 410, 2203
- Salim S., Lee J. C., Ly C., Brinchmann J., Davé R., Dickinson M., Salzer J. J., Charlot S., 2014, *ApJ*, 797, 126
- Salim S., Lee J. C., Davé R., Dickinson M., 2015, *ApJ*, 808, 25
- Salpeter E. E., 1955, *ApJ*, 121, 161
- Sánchez S. F. et al., 2012, *A&A*, 538, A8
- Sánchez S. F. et al., 2013, *A&A*, 554, A58
- Sánchez S. F. et al., 2017, *MNRAS*, 469, 2121
- Sanders R. L. et al., 2020, *MNRAS*, 491, 1427
- Sanders R. L. et al., 2021, *ApJ*, 914, 19
- Sanders R. L., Shapley A. E., Topping M. W., Reddy N. A., Brammer G. B., 2023, preprint (arXiv:2303.08149)
- Saracco P. et al., 2023, *MNRAS*, 520, 3027
- Savaglio S. et al., 2005, *ApJ*, 635, 260
- Schaefer A. L. et al., 2022, *ApJ*, 930, 160
- Scholte D., Saintonge A., 2022, *MNRAS*, 518, 353
- Sextl E., Kudritzki R.-P., Zahid H. J., Ho I.-T., 2023, *ApJ*, 949, 14
- Shapley A. E. et al., 2015, *ApJ*, 801, 88
- Sharda P., Krumholz M. R., Wisnioski E., Forbes J. C., Federrath C., Acharyya A., 2021, *MNRAS*, 502, 5935
- Simons R. C. et al., 2021, *ApJ*, 923, 203
- Sobral D., Best P. N., Matsuda Y., Smail I., Geach J. E., Cirasuolo M., 2012, *MNRAS*, 420, 1926
- Speagle J. S., Steinhardt C. L., Capak P. L., Silverman J. D., 2014, *ApJS*, 214, 15
- Spitoni E., Calura F., Matteucci F., Recchi S., 2010, *A&A*, 514, A73
- Spitoni E., Vincenzo F., Matteucci F., 2017, *A&A*, 599, A6
- Springel V. et al., 2005, *Nature*, 435, 629
- Stasińska G., 2005, *A&A*, 434, 507
- Steidel C. C. et al., 2014, *ApJ*, 795, 165
- Storey P. J., Zeppen C. J., 2000, *MNRAS*, 312, 813
- Stott J. P. et al., 2013, *MNRAS*, 436, 1130
- Stott J. P. et al., 2014, *MNRAS*, 443, 2695
- Stott J. P. et al., 2020, *MNRAS*, 497, 3083
- Suzuki T. L. et al., 2021, *ApJ*, 908, 15
- Teklu B. B., Gao Y., Kong X., Lin Z., Liang Z., 2020, *ApJ*, 897, 61
- Torrey P. et al., 2019, *MNRAS*
- Tremonti C. A. et al., 2004, *ApJ*, 613, 898
- Troncoso P. et al., 2014, *A&A*, 563, A58
- Trump J. R. et al., 2013, *ApJ*, 763, L6
- Wake D., 2016, in American Astronomical Society Meeting Abstracts #227, p. 334.01
- Wang X. et al., 2017, *ApJ*, 837, 89
- Wang X. et al., 2019, *ApJ*, 882, 94
- Wang X. et al., 2022, *ApJ*, 926, 70
- Wuyts E. et al., 2016, *ApJ*, 827, 74
- Yang N., Scholte D., Saintonge A., 2022, preprint (arXiv:2212.10657)
- Yates R. M., Kauffmann G., Guo Q., 2012, *MNRAS*, 422, 215
- Yates R. M., Hendriks D., Vijayan A. P., Izzard R. G., Thomas P. A., Das P., 2023, *MNRAS*, 527, 6292
- York D. G. et al., 2000, *AJ*, 120, 1579
- Zahid H. J., Dima G. I., Kudritzki R.-P., Kewley L. J., Geller M. J., Hwang H. S., Silverman J. D., Kashino D., 2014, *ApJ*, 791, 130

This paper has been typeset from a  $\text{\LaTeX}$  file prepared by the author.